Numerical Simulation of Stress Evolution in Lithium Manganese Dioxide Particles due to Coupled Phase Transition and Intercalation

Jonghyun Park,[a] Wei Lu,[a,z] and Ann Marie Sastry[a,b,c]

[a]Department of Mechanical Engineering, [b]Department of Biomedical Engineering, and [c]Department of Material Science and Engineering, University of Michigan, Ann Arbor, Michigan 48109-2125, USA

Lithium manganese dioxide particles undergo a significant volume change after transition from the cubic to the tetragonal phase. The transition may cause severe damage in cathode materials and capacity fade. This paper proposes a volume expansion and diffusion model to evaluate stresses due to phase transition. A three-dimensional finite element approach is developed to account for coupled phase transition and intercalation effects, which is applicable to arbitrary particle geometries. The study shows that the stress levels are closely related to particle geometry, lithium diffusivity, and input current density. The stress due to phase transition is roughly an order of magnitude higher than that due to intercalation in the cubic phase. However, the interaction kinetics still plays an important role on the stress distribution because it affects the concentration profile and emergence of phase transition. Lower diffusivity and higher current density induce a larger gradient in the lithium concentration and lead to higher stress levels.
© 2010 The Electrochemical Society. [DOI: 10.1149/1.3526597] All rights reserved.

Capacity fade in lithium-ion batteries is one of the critical problems that must be resolved to realize practical power sources for electrical vehicles. While the mechanism is related to a number of processes and their interactions, such as electrochemical, chemical, and mechanical degradation, the buildup of high stress is a critical issue. The high stress level may lead to mechanical fracture that can contribute to capacity fade in several ways. Fracture of the active electrode material can result in decreasing capacity due to its isolation from the electronically conducting matrix of the electrode. Fragmentation also affects the particle network and electrical resistance. The stress is typically caused by volume change due to intercalation. Many materials undergo large volume changes during intercalation and deintercalation of lithium ions into electrode materials,[1-3] and fractures on electrode material have been reported in several compounds, including graphite,[4,5] $LiCoO_2$,[6] $LiMn_2O_4$,[7-12] and $LiFePO_4$.[13,14] Fragmentation of $LiMn_2O_4$ particles during lithium insertion/deinsertion has been observed via various experimental techniques, including X-ray diffraction (XRD),[9] scanning electron microscopy (SEM),[7] tunneling electron microscopy (TEM),[9] NMR spectroscopy,[8,12] and acoustic emission spectroscopy (AES).[10,11]

In $Li_xMn_2O_4$ spinel systems, lithium is inserted into and extracted from the interstitial sites in the host Mn_2O_4 framework when $0 < x < 1$. During this process the cubic structure expands and contracts. The associated volume change induces stress that may lead to particle fracture. The volume change due to intercalation is about 6.5% in the cubic phase of $Li_xMn_2O_4$ when x changes from 0.2 to 0.995.[15] Two phases, cubic spinel $LiMn_2O_4$ and tetragonal $Li_2Mn_2O_4$, coexist when $1 < x < 2$. In cubic $LiMn_2O_4$, lithium occupies the tetrahedral sites, while in the tetragonal $Li_2Mn_2O_4$ lithium predominantly occupies the octahedral sites.[16,17] This first order transition combined with Jahn–Teller distortion results in a large volume change that can cause severe damage and fade in active materials.[16,18-20] Experimental study of the reduction of spinel-related manganese dioxide has shown that the change in the lattice from cubic to tetragonal involves 3% shrinkage in the *a*-axis and 12% expansion in the *c*-axis, resulting in 5.6% total expansion in unit cell volume.[16] Some experiments measured 6.6% expansion in volume when the phase changes from $LiMn_2O_4$ to $Li_2Mn_2O_4$.[15]

While strictly limiting the composition of $Li_xMn_2O_4$ within $0 < x < 1$ may prevent the onset of Jahn–Teller distortion in the spinel structure, experiments have shown that $Li/Li_xMn_2O_4$ cells still lose capacity when they are charged and discharged between 4.5 and 3.0 V. Phase boundaries separating the tetragonal phase at the surface of the crystallite from the cubic phase within the bulk was observed.[9] At high current density, some crystallites at the surface can be overlithiated and then undergo phase transition even above 3 V. This phase transition could be a problem for high power batteries being developed for electric vehicles.

Transition from the cubic to tetragonal phase has also been shown by temperature change, which happened at low temperature around $T_t = 280$ K.[20] With a structure of Fd3m at room temperature, the phase at low temperature below T_t was shown to be a mixture of Fd3m and I4$_1$/amd groups. The phase transition from Fd3m to I4$_1$/amd proceeded with the decrease in temperature until the volume fraction of the I4$_1$/amd phase saturated at 65% at around 260 K.

Recently several models have been developed to capture the stress due to lithium intercalation/deintercalation. A one-dimensional model was developed to estimate stress generation within spherical electrode particles.[21,22] Intercalation-induced stresses in particles with various three-dimensional (3D) shapes and sizes have been studied using finite elements,[23] where diffusion-induced stress was accounted for in analogy to thermal stress.[24-26] Analytical expressions were developed for stress evolution in spherically shaped electrode elements under galvanostatic or potentiostatic conditions.[27,28] A recent work showed a homogenization technique relating parameters in the microscale particle model to those in the macroscale model to explore the effects of an externally applied mechanical load.[29] The mechanical stresses in ideal spherical particles were coupled in a pseudo–two-dimensional (2D) porous electrode model at cell-scale to evaluate stresses in $LiCoO_2$/graphite cells.[30] To consider the stress due to phase transition, several researches have analytically calculated the stress generated in a spherical particle due to phase transition along the 3 V plateau.[31] The model considered ideal spherical particles expanded isotropically without including stress due to intercalation of lithium into the cubic phase. However, the latter is significant because it is closely related to kinetics such as current rate and diffusivity of lithium ions in the host structures.

Stress due to phase transition may increase significantly when it is combined with the volume change due to intercalation. Consequently, capturing the stress evolution during phase transition requires consideration of particle size, geometry, and intercalation kinetics. We propose to develop a model that predicts stresses in lithium manganese dioxide materials due to the intercalation of lithium and phase transition from the cubic to tetragonal phase. Spe-

cifically, we aim to elucidate how stress emerges in a nonspherical particle and how stress level relates to diffusivity, current density, and particle geometry.

Three-Dimensional Finite Element Approach for Coupled Phase Transition and Intercalation

Insertion of lithium into the Mn_2O_4 host structure starts with a single phase reaction where lithium occupies the tetrahedral sites. During this intercalation process lithium diffuses into the Mn_2O_4 particle, forming a concentration gradient profile that results in a stress field in the cubic $Li_xMn_2O_4$ phase ($0 < x < 1$). As the lithium concentration increases further and reaches the maximum stoichiometric, phase transition from the cubic $LiMn_2O_4$ to the tetragonal $Li_2Mn_2O_4$ occurs. We will consider both stages to capture stress evolution.

To obtain the concentration profile due to intercalation, we solve the diffusion problem together with the elastic field. The driving force for lithium-ion diffusion can be obtained by the gradient of the characteristic potential comprising the chemical and elastic energy of the system. The diffusion flux **J** is given by[23]

$$\mathbf{J} = -D\left(\nabla c - \frac{\Omega c}{RT}\nabla \sigma_h\right) \quad [1]$$

where c is the concentration of the lithium ion, D is the diffusion coefficient, R is the gas constant, T is the absolute temperature, σ_h is the hydrostatic stress, and Ω is the partial molar volume. The first term on the right-hand side accounts for the effect of the concentration gradient, where lithium ions diffuse to lower concentration regions from higher concentration regions. The second term accounts for the effect of the stress gradient. Lithium ions diffuse to regions with higher hydrostatic stress, where the stretching of the host makes it more difficult for the lithium to insert into the host material.

Combining Eq. 1 with the mass conservation equation, $\partial c/\partial t + \nabla \cdot \mathbf{J} = 0$, we have

$$\frac{\partial c}{\partial t} - \nabla \cdot \left[D\left(\nabla c - \frac{\Omega c}{RT}\nabla \sigma_h\right)\right] = 0 \quad [2]$$

The hydrostatic stress σ_h is obtained from the elastic field calculation. The diffusion, Eq. 2 is solved by a constant current boundary condition

$$\mathbf{J} \cdot \mathbf{n} = i_n/F \quad [3]$$

where **n** is the normal vector of the particle surface, i_n is the electric current density, and F is Faraday's constant.

The stress–strain relation with the effect of intercalation is given by

$$\varepsilon_{ij} = \frac{1}{E}[(1 + \nu)\sigma_{ij} - \nu\sigma_{kk}\delta_{ij}] + \frac{c\Omega}{3}\delta_{ij} \quad [4]$$

where ε_{ij} and σ_{ij} are strain and stress components, E is Young's modulus, ν is Poisson's ratio, c is the lithium ion concentration, and δ_{ij} is the Kronecker delta. The last term accounts for the intercalation strain. Note that Eq. 2 and 4 are coupled through the concentration c and the hydrostatic stress σ_h.

Volume change due to phase transition can be treated in analogy to thermal strain. The stress–strain relation in the tetragonal phase is given by

$$\varepsilon_{ij} = \frac{1}{E}[(1 + \nu)\sigma_{ij} - \nu\sigma_{kk}\delta_{ij}] + \frac{c\Omega}{3}\delta_{ij} + \frac{\omega_{CT}}{3}\delta_{ij} \quad [5]$$

where $\omega_{CT} = (V_T - V_C)/V_C$ is the percentage of volume change due to phase transition. Here V_T and V_C are the unit cell volumes of the tetragonal and cubic phase, respectively. Here we have assumed that the volumetric strain is isotropic. The Jahn–Teller distortion is anisotropic. However, the active particles are made up of a large number of compacted granular crystalline grains of spinel structures, that
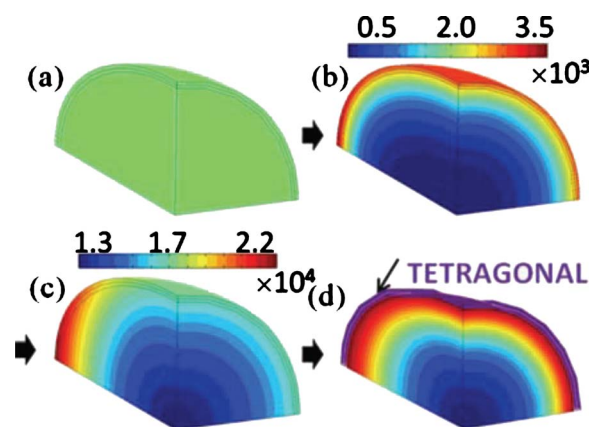
Figure 1. (Color online) Lithium concentration profile at representative steps: (a) Initial manganese dioxide particle, (b) Li-ion diffuses into the particle, forming a concentration profile, (c) the tip of the long axis reaches the stoichiometric maximum and phase transition starts to occur, and (d) formation of a tetragonal phase shell.

are measured in nanometers.[32,33] An SEM observation shows that powders contain agglomerated particles with an average grain size of about 50 nm.[34] As seen in many engineering materials, the orientation of crystalline and grain microstructure is distributed randomly so that macroscopic elastic properties are almost the same in all directions. Thus we assumed isotropic behavior, which is reasonable for the goal of the present work.

The coupled problem is solved in three-dimensional space using FEMLAB (COMSOL Multiphysics). Two models are included in the multiphysics simulation, the PDE (partial differential equation) model and the solid stress–strain model. In the PDE model, the diffusion process is described by the generalized form of Eq. 2. In the solid stress–strain model, "thermal expansion" is included as a load based on the variable of concentration c instead of temperature in the thermal stress calculation.

Our simulations show that the concentration at the tip of the long axis reaches the maximum stoichiometric concentration first, where the tetragonal phase starts to emerge. The interface between the tetragonal and cubic phases gradually migrates toward the cubic phase with more lithium ions diffusing into the particle. The moving velocity of an interface can be limited by the interface reaction or diffusion of Li ions to the interface. Here we consider the diffusion-controlled process, where the local reaction at the interface happens much faster so that diffusion limits the interface velocity. Calculated from the mass balance, the interface velocity, v, is given by

$$v = \frac{1}{C_{eq}^\beta - C_{eq}^\alpha}(D_\alpha \nabla C_\alpha \cdot \mathbf{n} - D_\beta \nabla C_\beta \cdot \mathbf{n}) \quad [6]$$

where C_α and C_β represent the concentration in the α and β phase, respectively, with D_α, D_α being the corresponding diffusion coefficients. C_{eq}^α and C_{eq}^β indicate the equilibrium concentration at the boundary and **n** represents the normal vector at the boundary. Equation 6 indicates that the volume of the new phase formed is related to the gradient of concentration and time of evolution. The approach we have taken to obtain the concentration profile and evaluate the shell thickness of the tetragonal phase in order to calculate the stress level is summarized below. Figure 1 shows the Li concentration profile at representative steps.

A simulation starts from an initial Mn_2O_4 phase (Fig. 1a). As lithium diffuses from the outside to the inside of the particle, a concentration distribution develops. Here the boundary condition is the Neumann boundary condition (constant flux). The regions closer to the long axis of the particle have higher lithium concentrations as can be seen in Fig. 1b. When the concentration in a region reaches the stoichiometric maximum, transition from the cubic to tetragonal

Table I. Material properties used in the simulation.

Name	Symbol and unit	Value
Young's modulus	E (GPa)	10 (Ref. 24)
Poisson's ratio	ν	0.3 (Ref. 24)
Diffusion coefficient	D_0 (m²/s)	7.08×10^{-15} (Ref. 23)
Stoichiometric maximum concentration	$c_{\max}$ (mol/m³)	2.29×10^4 (Ref. 20)

phase happens in that region (Fig. 1c). Then the interface velocity is calculated based on the concentration gradient. The calculated phase diagram shows that there is a large miscibility gap between $x = 1$ and 2 in $Li_xMn_2O_4$.[35] This gap disappears above approximately 450 K. Below $x = 1$, the lithium ions predominantly occupy the tetrahedral sites. As the lithium concentration is increased, the miscibility gap is entered, whereby $LiMn_2O_4$ coexists with $Li_xMn_2O_4$ with x slightly less than 2. The concentration of the tetragonal phase is fairly uniform around 2. For this reason, we ignore the gradient of the concentration at the tetragonal phase when evaluating the interface velocity. The tetragonal phase emerges from a zone at the tip of the long axis of the particle and gradually expands to the particle surface to form a complete shell. Here we calculate the maximum shell thickness in the long axis to be 1/20 of the long semiaxis, which is based on the observed thickness of the tetragonal phase layer.[9] Figure 1d shows the final configuration in order to evaluate the stresses in the system. The thickness of the tetragonal shell is not uniform, but is roughly proportional to the respective semiaxis lengths. The lattice expansion in the tetragonal phase is constant, which has been observed in XRD measurements.[16] This means that we can treat the volume expansion due to the formation of the tetragonal phase as independent of the concentration, as shown in Eq. 5. In contrast, the volume expansion of the cubic phase, where x is not fixed but can be anywhere from 0 to 1, is a function of concentration as shown in Eq. 4.

Simulation Parameters

To study the effect of aspect ratios on the stress level, ellipsoids with different aspect ratios were studied. The current density on the surface is fixed at $i_n = 2$ A/m². For the ellipsoid, the lengths of three semiaxes a, b, and c satisfy $a = b$, and the aspect ratio is defined as c/a. The volumes of the ellipsoids were fixed at $4\pi \times 5^3/3$ μm³. An aspect ratio of 1 corresponds to a spherical particle with a radius of 5 μm.

Considering the symmetry of the particle geometry, we performed simulations on 1/8 of the particle. Symmetric boundary conditions were applied on the planes of symmetry. We calculated the lithium diffusion until a shell of tetragonal phase formed. All material properties used in the simulations are listed in Table I with mechanical properties obtained from Ref. 36. The Young's modulus of $LiMn_2O_4$ has been measured experimentally using the vibrating-reed measurement[37] and anelastic spectroscopy.[36] The vibrating-reed method gives 25 GPa, while anelastic spectroscopy gives 10 GPa. As the authors of these measurements have mentioned, the chemical compositions of the samples are different. The sample composition for the vibrating-reed method was $Li_{0.95}Mn_2O_4$, while the correct stoichiometry of the sample used in anelastic spectroscopy was checked by means of redox titration. Even though the modulus from ab initio calculations is roughly an order of magnitude higher than that from experiments, the calculation showed only a slight variation of the modulus with state of charge (SOC) changes.[38] Several papers have used 10 GPa in their studies.[24,31,39] In the present work, we selected 10 GPa because our target material is similar to that used in the reported experiment and assumed independent of the amount of lithium content following the ab initio calculation. Some studies have used a modulus on the order of hundreds of gigapascal.[40] Young's modulus can be easily converted from one value to another.

We will compare results of three cases using 10, 25, and 100 GPa. Other parameters are $\Omega = 3.497 \times 10^{-6}$ (m³/mol) and $\omega_{CT} = 0.066$.[15]

Results and Discussion

The failure of brittle materials such as $Li_xMn_2O_4$ is closely related to the tensile stress.[41] We calculated the three principal stresses, σ_1, σ_2, and σ_3, in the particle and captured their evolution during lithium intercalation and phase transition. The maximum tensile stress at one point is given by σ_1 after ordering the three principal stresses in descending order (σ_3 being the smallest).

Figure 2 shows results for a particle with an aspect ratio of 1.95. Figure 2a shows the evolution of the maximum principal stress σ_1 in the particle until phase transition (phase transition happens at a time of about 1152 s). The stress level increases during the first 600 s, followed by a slight decrease. The stress level is determined by both the concentration gradient and the amount of intercalated Li ions. In the later stage the concentration gradient is reduced significantly, causing the stress level to drop. Thus the stress level reaches the highest in the middle of the discharge process rather than at the end. The 3D image within Fig. 2a shows the lithium concentration profile at 600 s. The concentration varies from low in the particle center to high on the particle surface, which suggests that the outer part of the particle expands more. As a result, the center part of the particle is under tension while the outer part is under compression. The lithium concentration at the tip of the long axis (Q) is larger than that at the tip of the short axis (P), while the compressive principal stress level at P is larger than that at Q due to larger concentration gradient, as shown by the 3D image on the left-side in Fig. 2c.

Figure 2b shows the maximum σ_1 before and after phase transition with and without intercalation. The latter was calculated by assuming no diffusion in the cubic phase (thus no volume expansion) and simply replacing the outer shell of the particle with the tetragonal phase. The volume and distribution of the tetragonal phase are identical in the comparison. The difference in the maximum σ_1 clearly shows the importance of considering the lithium gradient in the cubic phase. Also note that in the two cases the maximum σ_1 happens at different locations. The maximum σ_1 considering volume mismatch due to only phase transition happens at the tip of the long-axis of the cubic phase. In contract, the maximum σ_1 happens in the center of the particle when considering both intercalation and phase transition. Again, the concentration gradient in the cubic phase makes a difference. After phase transition the stress σ_1 jumps from 52 to 132 MPa due to an abrupt volume expansion. Unlike the intercalation-induced stress, phase transition produces an abrupt change in the stress level and a large compressive principal stress in the tetragonal phase.

While a brittle material is sensitive to tensile stress, a large compressive stress may also cause failure. Thus Fig. 2c shows the distribution of σ_3 before and after phase transition. A significant compressive stress with magnitude larger than 350 MPa emerges at the tip of the short axis of the tetragonal phase. This magnitude is much higher than the maximum tensile stress (132 MPa) in the particle. On the other hand, the compressive strength of a ceramic is typically much higher than the tensile strength. As a result, failure may first appear at either the tetragonal phase or the cubic phase depending on the material properties. To the best of our knowledge, systematic measurements of the tensile and compressive strengths of lithium manganese oxide have not been reported. Silicon nitride has a tensile strength of 100–150 MPa (Ref. 42) and rutile TiO_2 has a tensile strength between 69 and 103 MPa.[43] It is expected that the strength is dependent on the synthesis process, which affects the distribution of defects such as microcracks. As a rough estimate, we assume that the tensile strength of the lithium manganese particle is $\sim$100 MPa and the compressive strength is much higher.[31] The stress level after phase transition has surpassed this value, suggesting that the stress due to phase transition is sufficient to cause failure.
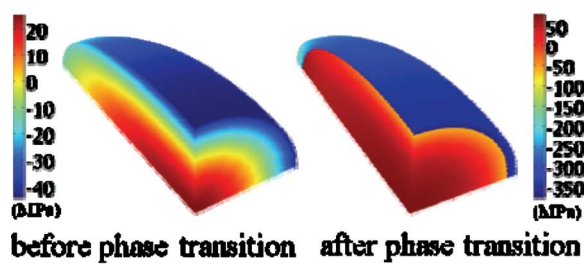
The diffusivity of lithium ions in the particle affects the stress
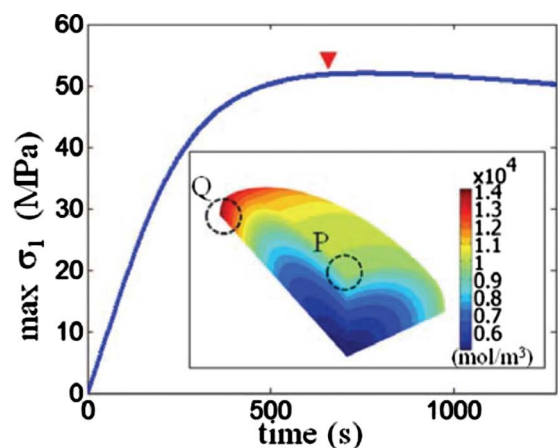
(a)
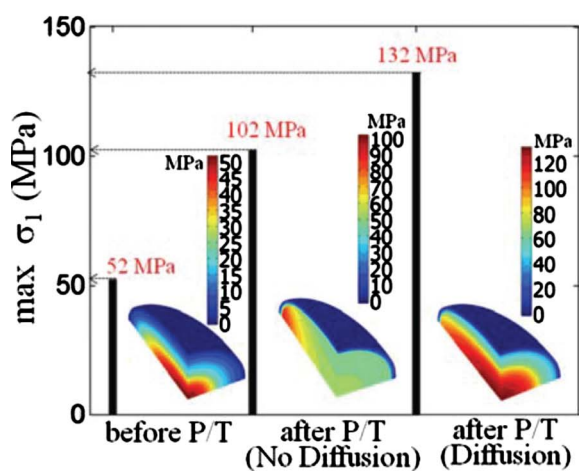
(b)

(c)

Figure 2. (Color online) Intercalation and phase transition induced stress in a particle with an aspect ratio of 1.95. (a) Evolution of the maximum principal stress σ_1 in the particle. The 3D image shows the lithium concentration profile at 600 s, when the stress level is maximized. (b) Comparison of the maximum σ_1 before and after phase transition without and with intercalation. The 3D images show σ_1 distribution in the particle. (c) σ_3 distribution in the particle before and after phase transition.

level because the concentration profile is closely related to the stress field. At the same time, the stress field affects the diffusion of ions. An intercalated lithium ion displaces the host atoms and a stress field builds up in the host structure. This stress field affects the energy of a second intercalated ion, leading to an elastic interaction between the two ions. Figure 3 shows the maximum σ_1 at different diffusivity. The 3D images in the figure show the concentration profile. When $D = 5D_0$, the concentration inside a particle is larger, while the concentration gradient is smaller. Due to the coupling of
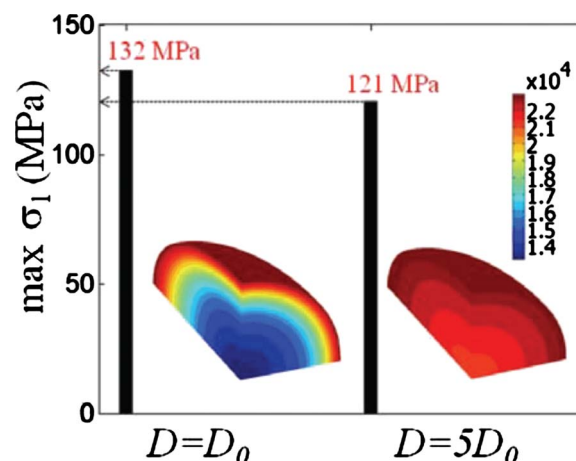

Figure 3. (Color online) The effect of lithium diffusivity on the stress level. The black bars represent the maximum σ_1. The 3D images show the lithium concentration profile.

concentration and stress, varying the diffusivity results in different maximum principal stress levels and distribution patterns after phase transition. For the case of higher diffusivity, the smaller concentration gradient leads to lower intercalation stress before phase transition. For the case of lower diffusivity, the concentration gradient in the thickness direction is much larger, so that the stress due to intercalation still contributes a significant portion after phase transition and leads to higher stress levels.

We have investigated the effect of Young's modulus by using three different values, 10, 25, and 100 GPa, for a particle with an aspect ratio of 1.95. Figure 4 shows the simulation results. The stress level shows a significant change and scales with the modulus. The results suggest that the elastic modulus of lithium manganese oxide has an important effect on the stress level, and its precise experimental measurement is technically significant. The time it takes to form a tetragonal phase shell also depends on the modulus. Larger modulus induces higher intercalation stress which slows down the diffusion.

The current density on the surface of a particle depends on the C-rate, as well as the location of the particle in the electrode. The current density is higher for a particle near the separator. To elucidate the effect of current density on the maximum stress level, we have conducted simulations at various current densities for a particle with an aspect ratio of 2.92. For this particle the conversation relation is 5 A/m² equal to 6C. Figure 5a shows the effect of input
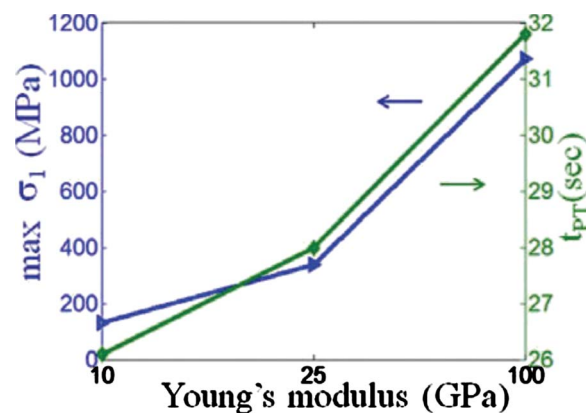
Figure 4. (Color online) The effect of Young's modulus on the stress level. The blue curve shows the maximum σ_1 while the green curve shows the time (t_{PT}) to form the tetragonal phase shell.
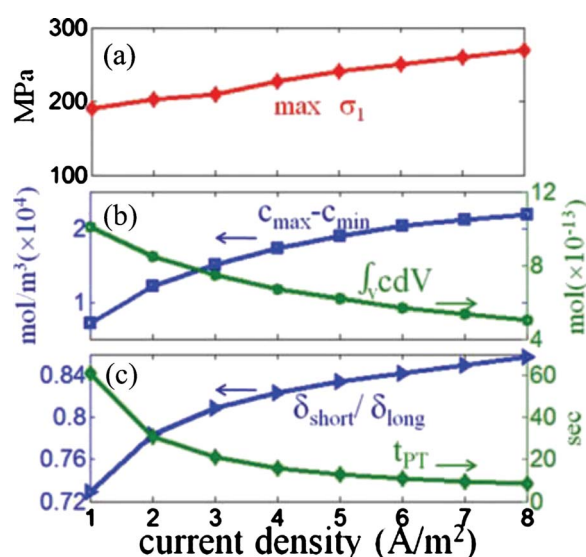
Figure 5. (Color online) The effect of the input current density on (a) maximum σ_1, (b) the difference between the maximum and minimum concentrations in the particle (blue curve) and total intercalated lithium ions (green curve), (c) the shape of the tetragonal phase shell (blue curve: δ_{short}, shell thickness in the direction of the short axis; δ_{long}, shell thickness in the direction of the long axis), and the time (t_{PT}) it takes to form the tetragonal phase shell (green curve). Results for a particle with an aspect ratio of 2.92.

Figure 6. (Color online) The effect of the tetragonal phase shell thickness on the stress level. The black bars represent the maximum σ_1. The 3D images show the lithium concentration profile. The shell thickness in the long direction is 1/20 and 1/10 of the long semiaxis. Results for a particle with an aspect ratio of 2.92.

calation. This observation means that when a particle undergoes phase transition due to either a lower voltage under 3 V or a fast discharge at a higher voltage over 3 V, the stress developed on a phase boundary may cause structural failure. Parametric studies on
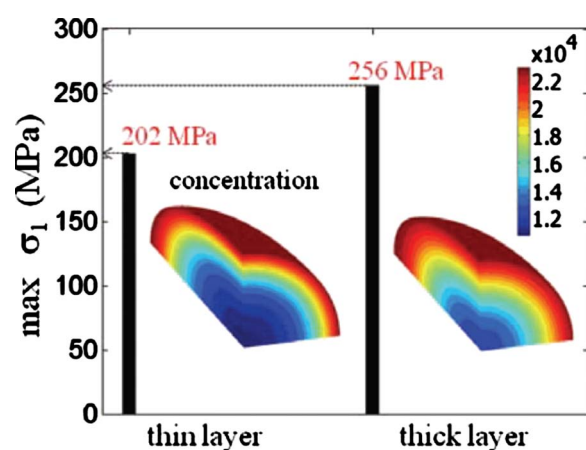
current density on the maximum principal stress. A higher current density results in a higher stress level, but the increase slows down. Figure 5b shows that a higher input current density induces a higher gradient in the lithium concentration. However, the total amount of lithium intercalated (until the concentration reaches the stoichiometric maximum) is larger with a lower current density. This behavior is because a high current density quickly causes an outer layer of cubic phase to transform into a shell of tetragonal phase, before Li ions have much time to diffuse into the particle. The current density also affects the shape of the tetragonal phase shell and the time it takes to form the shell, as shown in Fig. 5c. A higher current results in a thicker shell along the short axis (the shell thickness in the long axis is targeted at 1/20 of the long semiaxis). The formation of the shell is also much faster. Thus a high discharge rate may cause an unintended phase transition.

Figure 6 shows the effect of the tetragonal phase shell thickness on the stress level. Two cases are compared, where the shell thickness in the long direction is 1/20 and 1/10 of the long semiaxis, respectively. A thick layer causes a higher tensile stress level. The 3D images show the concentration profile. The longer diffusion time associated with the formation of a thicker shell leads to a lower concentration gradient.

Figure 7 shows the geometric effect on the stress level at a discharge rate of 2C. In Fig. 7a, the green line represents the maximum stress due to intercalation before phase transition. The stress level increases first and then decreases with the aspect ratio. This behavior is consistent with the results from previous work.[23] However, the maximum stress due to phase transition, represented by the blue line, does not follow this trend. Representative σ_1 distribution in particles is shown in Fig. 7b. These results suggest that particle shape is an important factor that affects the stress level, and thus affects the reliability.
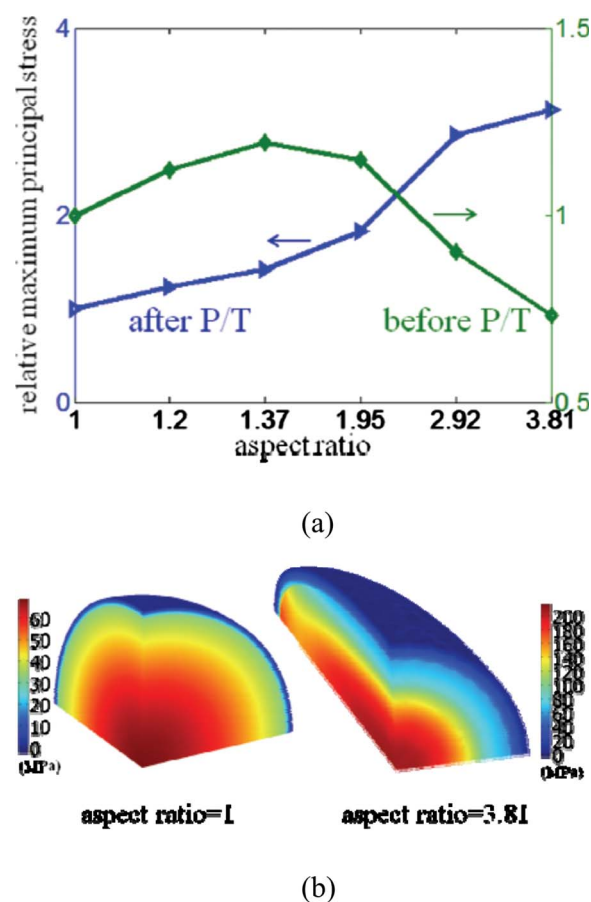
Conclusion

In this work stresses due to phase transition and intercalation are calculated. By considering concentration gradients in a cubic phase before phase transition, we are able to include the kinetics related to current rate and diffusivity of lithium ions. Simulations demonstrate that the stress due to phase transition is larger than that from inter-

(a)

(b)

Figure 7. (Color online) The effect of particle geometry on the stress level. (a) The blue and green curves show the ratio of the maximum σ_1 relative to the value at an aspect ratio of 1 after and before phase transition, respectively. (b) The distributions of σ_1 in two particles with aspect ratios of 1 and 3.81.

diffusivity, current input density, shell thickness, and the shape of particles reveal that the maximum stress level and stress distribution are determined by the lithium concentration in the cubic phase and by particle geometry, both of which are critical during the phase transition.

References

1. G. Pistoia, M. Pasquali, L. A. de Picciotto, and M. M. Thackeray, *Solid State Ionics*, **28**, 879 (1988).
2. R. J. Cava, D. W. Murphy, S. Zahurak, A. Santoro, and R. S. Roth, *J. Solid State Chem.*, **53**, 64 (1984).
3. M. G. S. R. Thomas, W. I. F. David, J. B. Goodenough, and P. Groves, *Mater. Res. Bull.*, **20**, 1137 (1985).
4. R. Kostecki and F. McLarnon, *J. Power Sources*, **550**, 119 (2003).
5. M. Markervich, G. Salitra, M. D. Levi, and D. Aurbach, *J. Power Sources*, **146**, 146 (2005).
6. H. Wang, Y. Jang, B. Huang, D. R. Sadoway, and Y.-M. Chiang, *J. Electrochem. Soc.*, **146**, 473 (1999).
7. M.-R. Lim, W.-I. Cho, and K.-B. Kim, *J. Power Sources*, **92**, 168 (2001).
8. M. C. Tucker, J. A. Reimer, and E. J. Cairns, *J. Electrochem. Soc.*, **149**, A574 (2002).
9. M. M. Thackeray, Y. Shao-Horn, A. J. Kahaian, K. D. Kepler, E. Skinner, J. T. Vaughery, and S. A. Hackney, *Electrochem. Solid-State Lett.*, **1**, 7 (1998).
10. T. Ohzuku, M. Kitagawa, and T. Hirai, *J. Electrochem. Soc.*, **136**, 3169 (1989).
11. T. Ohzuku, H. Tomura, and K. Sawai, *J. Electrochem. Soc.*, **144**, 3496 (1997).
12. M. C. Tucker, J. A. Reimer, and E. J. Cairns, *Electrochem. Solid-State Lett.*, **3**, 463 (2000).
13. D. Wang, X. Wu, Z. Wang, and L. Chen, *J. Power Sources*, **140**, 125 (2005).
14. H. Gabrisch, J. Wilcox, and M. M. Doeff, *Electrochem. Solid-State Lett.*, **11**, A25 (2008).
15. W. I. F. David, M. M. Thackeray, L. A. de Piccitotto, and J. B. Goodenough, *J. Solid State Chem.*, **67**, 316 (1987).
16. T. Ohzuku, M. Kitagawa, and T. Hirai, *J. Electrochem. Soc.*, **137**, 769 (1990).
17. M. M. Thackeray, *Prog. Solid State Chem.*, **25**, 1 (1997).
18. M. M. Thackeray, W. I. F. David, P. G. Bruce, and J. B. Goodenough, *Mater. Res. Bull.*, **18**, 461 (1983).
19. M. M. Thackeray, P. J. Johnson, L. A. de Picciotto, P. G. Bruce, and J. B. Goodenough, *Mater. Res. Bull.*, **19**, 179 (1984).
20. A. Yamada and M. Tanaka, *Mater. Res. Bull.*, **30**, 715 (1995).
21. K. Zaghib, J. Shim, A. Guerfi, P. Charest, and K. A. Striebel, *Electrochem. Solid-State Lett.*, **8**, A207 (2005).
22. J. Christensen and J. Newman, *J. Solid State Electrochem.*, **10**, 293 (2006).
23. X. Zhang, W. Shyy, and A. M. Sastry, *J. Electrochem. Soc.*, **154**, A910 (2007).
24. S. Prussin, *J. Appl. Phys.*, **32**, 1876 (1961).
25. J. C. M. Li, *Metall. Trans. A*, **9A**, 1353 (1978).
26. F. Yang, *Mater. Sci. Eng., A*, **409**, 153 (2005).
27. Y.-T. Cheng and M. W. Verbrugge, *J. Appl. Phys.*, **104**, 083521 (2008).
28. Y.-T. Cheng and M. W. Verbrugge, *J. Power Sources*, **190**, 453 (2009).
29. S. Golmon, K. Maute, and M. L. Dunn, *Comput. Struct.*, **87**, 1567 (2009).
30. S. Renganathan, G. Sikha, S. Santhanagopalan, and R. E. White, *J. Electrochem. Soc.*, **17**, A155 (2010).
31. J. Christensen and J. Newman, *J. Electrochem. Soc.*, **153**, A1019 (2006).
32. X. He, J. Li, Y. Cai, C. Jiang, and C. Wan, *Mater. Chem. Phys.*, **95**, 105 (2006).
33. Y. Iriyama, Y. Tachibana, R. Sasasoka, N. Kuwata, T. Abea, M. Inaba, A. Tasaka, K. Kikuchi, J. Kawamura, and Z. Ogumia, *J. Power Sources*, **174**, 1057 (2007).
34. Y.-K. Sun, I.-H. Oh, and K. Y. Kim, *Ind. Eng. Chem. Res.*, **36**, 4839 (1997).
35. A. V. de Ven, C. Marianetti, D. Morgan, and G. Ceder, *Solid State Ionics*, **135**, 21 (2000).
36. A. Paolone, R. Cantelli, G. Rousse, and C. Masquelier, *J. Phys. Condens. Matter*, **15**, 457 (2003).
37. J. Sugiyama, T. Tamura, and H. Yamauchi, *J. Phys. Condens. Matter*, **7**, 9755 (1995).
38. G. E. Crechnev, R. Ahuja, B. Johansson, and O. Eriksson, *Phys. Rev. B*, **65**, 174408 (2002).
39. X. Zhang, A. M. Sastry, and W. Shyy, *J. Electrochem. Soc.*, **155**, A542 (2008).
40. W. H. Woodford, Y. M. Chiang, and W. C. Carter, *J. Electrochem. Soc.*, **157**, A1052 (2010).
41. N. E. Dowling, *Mechanical Behavior of Materials*, Prentice-Hall, Englewood Cliffs, NJ (1999).
42. G. A. Gogotsi, G. G. Gnesin, Ya. L. Grushevskii, and V. P. Zavada, *Strength Mater.*, **19**, 674 (1988).
43. F. Cardarelli, *Materials Handbook: A Concise Desktop Reference*, Springer-Verlag, London (2000).